High-Resolution Automotive Imaging Using MIMO Radar and Doppler Beam Sharpening

Cassidy, Scott L.; Pooni, Sukhjit; Cherniakov, Mikhail; Hoare, Edward G.; Gashinova, Marina S.

DOI:
10.1109/TAES.2022.3203953

Document Version
Peer reviewed version

Citation for published version (Harvard):
Cassidy, SL, Pooni, S, Cherniakov, M, Hoare, EG & Gashinova, MS 2023, 'High-Resolution Automotive Imaging Using MIMO Radar and Doppler Beam Sharpening', *IEEE Transactions on Aerospace and Electronic Systems*, vol. 59, no. 2, pp. 1495-1505. https://doi.org/10.1109/TAES.2022.3203953

High resolution automotive imaging using MIMO radar and Doppler beam sharpening

Scott L. Cassidy
Sukhjit Pooni
Mikhail Cherniakov
Edward G. Hoare
Marina S. Gashinova
University of Birmingham, United Kingdom

***Abstract*— Highly detailed sensing of a vehicle's surrounding environment is a key requirement for the advancement of au-tonomous driving technology. While conventional automotive radar sensors remain robust under challenging weather conditions, poor cross-range resolution and high sidelobe levels present significant challenges. In this paper we propose an approach which combines MIMO beamforming with Doppler beam sharpening. We demon-strate a significant improvement in terms of cross-range resolution and, importantly, nearly 20 dB sidelobe suppression compared to conventional MIMO processing. This approach is investigated in detail and validated through theoretical analysis, simulation and experiment using data recorded on a moving vehicle. We demonstrate performance which is comparable to a high resolution mechanically scanned radar, using a commercially available MIMO sensor.**

***Index Terms*— automotive radar, millimeter wave radar,radar imaging, Doppler beam sharpening.**

I. INTRODUCTION

AUTOMOTIVE radar is perhaps the most pervasive and rapidly-developing civilian application of radar today. While there is a long history of research in the field [1], it is only in the last decade or so that the technology has seen wide adoption in the market, quickly transitioning from a luxury convenience to a critical safety feature [2]. This has been enabled in part by the availability of low-cost sensors using multiple-input multiple-output (MIMO) antenna designs [3], as well as the development of low-cost single chip radar transceivers [4]. Today there are a number of different commercial chipsets available and the technology continues to advance rapidly.

This research was funded in whole or in part by Innovate UK Grant 104268. For the purpose of open access, a CC BY public copyright licence is applied to any AAM arising from this submission.

Authors are with the Department of Electronic, Electrical and Systems Engineering, University of Birmingham, Birmingham, B15 2TT, United Kingdom. *(Corresponding author: S. L. Cassidy).*

Current consumer systems focus only on relatively simple convenience and safety functions such as automatic cruise control (ACC) and automatic emergency braking (AEB), where continuous monitoring of the vehicle surroundings is required for collision prevention and mitigation. Such functions fall into the category of Level 2 driving automation. These systems will become even more common in the coming years as AEB becomes mandatory in new cars in a number of important markets.

With the current push towards the development of self-driving vehicles, designated as Level 4/5 driving automation, there is a need for far more detailed sensing of the surrounding environment, in order to perform path planning and to adapt to changes in road layout such as road works [5]. In the current state-of-the-art, this is typically performed using optical cameras and lidar. However, these sensors can perform poorly under challenging weather conditions, such as heavy rain and fog [6], which must be addressed if this technology is to see widespread application. Radar has great potential to provide the required capabilities [7] while remaining robust under difficult weather conditions, particularly as part of a multi-sensor suite. There are, however, a number of challenges which must be properly overcome in order to achieve suitable performance. The most notable issues include poor cross-range resolution, high side-lobe levels and low dynamic range.

Early automotive sensors used either a patch and lens design or a mechanically scanned antenna. Mechanically scanned radars were reliable and offered good performance in terms of sidelobes, beamwidth and field-of-view. However, concerns about cost, update rate, weight and packaging requirements have driven the transition to electronic scanning as the only commercially viable solution. Additionally, electronic beam forming brings the advantage of higher frame rate and also permits continuous Doppler processing of the whole scene due to the constant illumination of the entire sensor field-of-view (FOV). MIMO designs are popular since the same resolution can be achieved with a smaller number of transmit and receive elements when compared to a full phased array.

Unlike a mechanically steered radar, but similar to electronic scanning, the beamwidth of a MIMO array increases off-boresight due to aperture foreshortening. Additionally, due to the broad illumination inherent to the MIMO technique, beamforming performance is equivalent to one-way propagation, and so does not benefit from the side-lobe suppression observed with two-way propagation [3]. In practice, performance can be degraded further below the theoretical expectations, for example by phase and amplitude errors across the array, though this may be partially mitigated by more effective calibration [8]. High sidelobe levels must be addressed as they cause severe performance degradation in imaging applications, especially in crowded urban environments.

The MIMO beamforming technique produces a virtual receiver array where each individual virtual array element

is synthesized by associating the signals from different pairs of transmit and receive elements. There are a number of different transmitter multiplexing techniques which have been proposed in order to achieve this [9]. One of the simplest and most common techniques is time-division multiplexing (TDM-MIMO), where each transmitter is activated individually in sequence. Under motion, an ambiguity exists between the target Doppler shift and the direction of arrival (DOA) dependent phase gradient at the array. A number of methods have been proposed to address this through hardware design or by other means [10], [11], [12].

Doppler beam sharpening (DBS), also known as unfocused synthetic aperture radar (SAR), allows for finer cross-range resolution than that of the real aperture by performing Doppler processing and exploiting the angular dependence of the radial velocity of a stationary target when the radar platform is moving [13]. DBS is well-established in airborne radar [14], but has thus far seen little application in automotive radar. Application of DBS for height-estimation in a 1D MIMO array has been reported [15]. Additionally, use of DBS for high resolution automotive imaging using a single fixed wide-beam antenna has previously been demonstrated at 300 GHz [16].

In this paper we propose the combination of DBS and MIMO for the purpose of both azimuth refinement and sidelobe suppression, to achieve good imaging performance of the stationary environment around the vehicle. By combining two independent angle estimation methods to obtain one single measure we demonstrate increased cross-range resolution across most of the of the FOV. Furthermore, since the majority of sidelobes will not overlap when combined, sidelobe levels will also be suppressed. This is similar to the improvement observed in a two-way beam pattern compared to a one-way beam pattern. Authors have filed a patent application for this combined MIMO-DBS approach [17].

For a constant coherent integration period, the beamwidth achieved by DBS decreases with the angle between the target and the vehicle velocity vector, due to the larger change in target radial velocity. Since MIMO beamwidth is minimized on-boresight, i.e. in the opposite sense, the DBS technique can be viewed as highly complementary.

While the MIMO-DBS technique presented in this paper could be extended to the case of moving targets, we have chosen to focus initially on the imaging of the stationary environment surrounding the vehicle.

This paper is organized as follows: Section II provides an overview of the MIMO technique as applied in the automotive application. Section III provides an overview of the DBS technique, describes the proposed MIMO-DBS processing approach and the expected level of performance as a function of hardware and signal processing parameters. Section IV provides results of both simulation and experiment with real on-vehicle data acquired using an Inras RadarLog 4TX/16RX MIMO sensor operating at 77 GHz [18], before and after MIMO-DBS processing. For a comparison, data was also recorded with PolaRAD, an experimental mechanically steered radar [7]. Finally, conclusions will be drawn and next steps discussed.

II. MIMO BEAMFORMING

A. Principles

The MIMO beamforming technique synthesizes a virtual receiver array from a smaller number of transmit and receive elements than for the equivalent fully populated array [3]. Each individual virtual array element is associated with a unique transmit and receive element pairing. In effect, synthetic copies of the receive array are created at offsets determined by the transmitter spacing. An array with M transmit elements and N receive elements will therefore produce a virtual array with a total of $M \cdot N$ elements. Fig. 1 illustrates this principle for the simplified case of a one-dimensional 2TX/2RX array, where the positions of the additional virtual receive elements are shown as dashed lines.

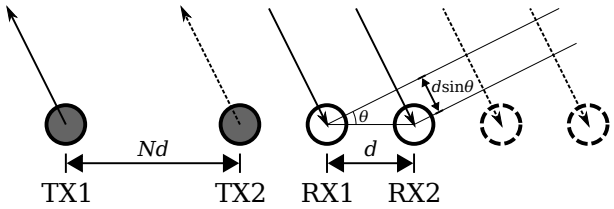

Fig. 1: Antenna arrangement of a one dimensional 2TX/2RX MIMO array (solid lines) and the equivalent virtual receive array (unshaded elements).

In the case of a regularly spaced virtual array with element separation d, and for a target located in the far-field of the array at an angle θ with respect to the boresight direction, the difference in path length between two adjacent virtual array elements is $d \sin\theta$. Hence, the complex signal observed at each element n is given by

$$s_n = \exp(j\omega n) \tag{1}$$

where ω is the phase difference observed between two adjacent array elements:

$$\omega = \frac{2\pi}{\lambda_c} d \sin\theta \tag{2}$$

where λ_c is the carrier wavelength. Beamforming can be performed efficiently by applying an FFT across the array, allowing multiple targets to be resolved in angle as

$$\theta = \arcsin\left(\frac{\omega\lambda_c}{2\pi d}\right) \tag{3}$$

The unambiguously resolvable angle is determined by the virtual array spacing, according to the Nyquist sampling criteria. A spacing of $\lambda_c/2$ satisfies Nyquist over the entire field-of-view.

Doppler processing is typically achieved by performing an FFT in slow time over number of MIMO frames.

The resulting velocity resolution and maximum unambiguously resolvable velocity are then defined as

$$\Delta v \approx \frac{\lambda_c}{2T} \tag{4}$$

$$v_{\max} \approx \pm \frac{\lambda_c}{4T_{\mathrm{MIMO}}} \tag{5}$$

where T is the total coherent processing interval (CPI) and T_{MIMO} is the MIMO frame interval, the period from the beginning of one TDM-MIMO sequence to the next.

B. Multiplexing and motion degradation

A number of methods have been proposed for transmitter multiplexing. Among these, TDM-MIMO has seen widespread adoption due to ease of implementation in hardware. Under TDM-MIMO, each transmitter is activated in sequence over a series of chirps. While this method achieves good orthogonality, a phase shift is introduced under platform motion due to the non-simultaneous capture of signals from each transmitter [10], [11], [12]. The phase shift introduced for transmitter n is given by

$$\Delta\phi_n = \frac{4\pi v_{\mathrm{r}} T_{\mathrm{chirp}} n}{\lambda_{\mathrm{c}}} \tag{6}$$

where v_{r} is the radial velocity of the target and T_{chirp} is the pulse repetition interval (PRI). The effect of this phase shift is to introduce step discontinuities to the phase observed across the array, which would be expected to have a fixed gradient in the case of a single point reflector. This has three consequences: error in measured angle of arrival, splitting of the main lobe into two separate lobes (i.e. one false target) and elevated side-lobe levels.

Given the periodic nature of (6), it is useful to define a normalized radial velocity

$$v'_{\mathrm{r}} = \frac{2T_{\mathrm{chirp}}}{\lambda_{\mathrm{c}}} v_{\mathrm{r}} \tag{7}$$

such that $\Delta\phi_n$ is a multiple of 2π when the value of v'_{r} is an integer. Fig. 2 shows the result of simulation of the azimuth profile for a 4TX/16RX MIMO array and a single target moving radially, as a function of v'_{r} with no weighting applied prior to beamforming.

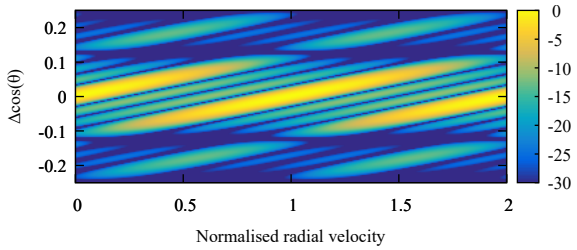

Fig. 2: Simulated azimuth profile for a single target as a function of v'_{r}. Splitting of the main lobe and additional false targets are visible at non-integer values of v'_{r}.

C. Motion compensation

Since the motion-induced degradation is dependent on the target radial velocity, correction must be performed in the Doppler domain. In order to apply motion compensation an estimate for v_r is also required, allowing $\Delta\phi_n$ to be calculated and subtracted from s_n by multiplying by $\exp(-j\Delta\phi_n)$ prior to beamforming. Since the phase error wraps through 2π periodically with velocity, we need not know the true platform velocity. It is sufficient to know the phase error modulo 2π. However, since the Doppler transform is typically performed in slow time, with a period equal to that of the full TDM-MIMO sequence, an ambiguity does exist since the inter-chirp period is smaller by a factor at least equal to the number of transmitters.

Increasing the pulse repetition frequency (PRF) to eliminate velocity ambiguity completely is often not feasible in current radar chipsets. Since this paper concerns the imaging of stationary targets only, it is reasonable to resolve the ambiguity under this assumption. A best-estimate of the true radial velocity in each velocity bin is obtained by resolving the Doppler ambiguity in favour of the value which lies closest to the platform velocity. This corresponds to the angular position closest to boresight. This is appropriate since, in practice, the radar FOV is limited by the the beam pattern of the physical antenna elements. The estimate will be accurate as long as there is no ambiguity in radial velocity within this FOV.

Fig. 3 shows the outcome of the phase error correction prior to beamforming for a real measurement of a complex road scene using an Inras RadarLog 4x16 MIMO sensor. Despite application of a Hann weighting function maximum azimuth sidelobes level is around -15 dB, due to difficulty in calibrating the array. Further results are shown in Section IV.

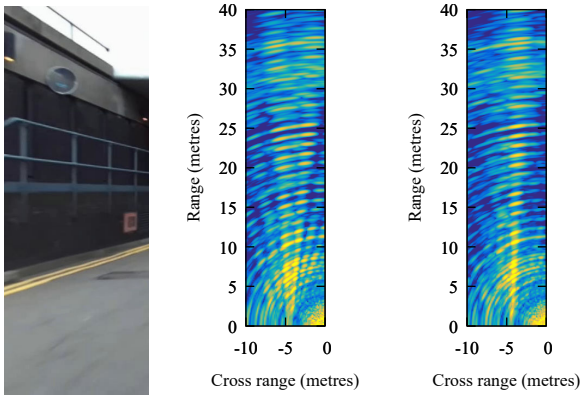

Fig. 3: Radar image before and after motion correction. The visible splitting of targets is eliminated after correction.

III. DOPPLER BEAM SHARPENING

A. Principles

Doppler beam sharpening (DBS) allows angular resolution to be increased beyond that of the physical antenna by exploiting the angular dependence of a stationary target's radial velocity when the platform is moving with a constant velocity [13]. Fig. 4 illustrates the underlying geometry and relative target velocity, assuming platform motion in the positive z direction.

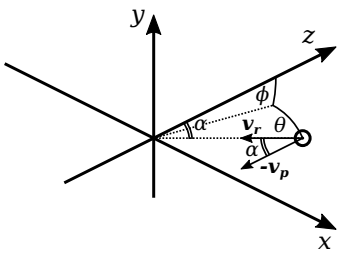

Fig. 4: Diagram showing geometry and relative velocity vectors for a single stationary point target. The radar is located at **0** and is directed along the z-axis.

By performing Doppler processing, the radial velocity of the target can be measured. Under the arrangement described above, the radial velocity is defined as

$$v_{\mathrm{r}} = -\boldsymbol{v}_{\mathrm{p}} \cdot \hat{\boldsymbol{r}} = -|\boldsymbol{v}_{\mathrm{p}}| \cos(\alpha) \tag{8}$$

where $\boldsymbol{v}_{\mathrm{p}}$ is the platform velocity vector, $\hat{\boldsymbol{r}}$ is the target unit position vector and α is the angle between the target position vector and the platform velocity vector. By calculating α we obtain the apex angle of a cone which intersects the true target position.

B. Combined MIMO and DBS processing

In a real-aperture radar, two-way propagation results in a narrower main lobe and reduced side-lobe levels compared to the one-way antenna pattern. Similarly, by combining MIMO and DBS, increased resolution and side-lobe suppression can be achieved across much of the radar field of view.

Fig. 5 shows the result of applying MIMO and DBS to a series of simulated point targets distributed in azimuth.

The DBS angle α obeys the following relation

$$\cos\alpha = \cos\theta \cos\phi \tag{9}$$

where ϕ is the angle of elevation. For a 2D array, this expression can be used directly. However, for the case of a 1D array where a direct measurement of ϕ is not available processing could be performed for a number of different values of ϕ thus obtaining some elevation resolution. For simplicity we shall consider targets for which ϕ is close to zero, in which case (9) simplifies to

$$\alpha \approx |\theta| \tag{10}$$

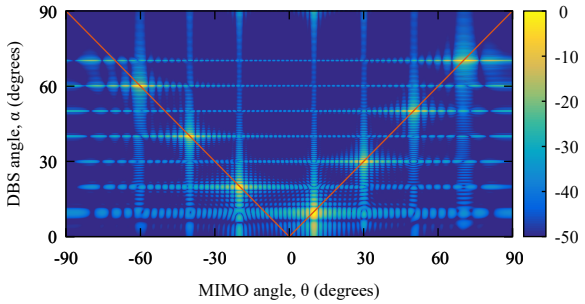

Fig. 5: Simulated plots showing (a) MIMO and DBS angle for targets at $\phi = 0$ and θ of -60°, -40°, -20°, 10°, 30°, 50° and 70°, with $\alpha = |\theta|$ shown as a red line.

Fig. 6 shows the sample density for both MIMO and DBS measurements. By extracting points located on this line we can successfully combine the MIMO and DBS measurements, reducing the dimensionality of the resultant radar datacube by one in the process. However, since these samples are non-uniformly and non-identically distributed, it is necessary to first convert to a common coordinate system. We employ a combination of zero padding for efficient interpolation in each dimension followed by an additional linear interpolation to obtain uniformly gridded data.

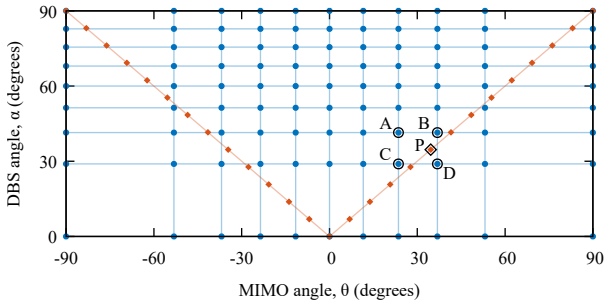

Fig. 6: Plot showing sample density for MIMO and DBS angles and after interpolation. Point P results from interpolation of points A, B, C and D. The number of sample points shown is reduced for the sake of clarity.

Fig. 7 shows the result of applying this process to simulated data, resulting in superior resolution compared to MIMO alone. Furthermore, it can clearly be seen that where MIMO and Doppler side-lobes do not coincide with the red line shown in Fig. 5 they are suppressed. This is particularly useful, given the high side-lobe levels inherent to MIMO, usually limited by the array calibration, even when weighting is performed prior to the FFT.

By differentiation of (8) it is clear that DBS angular resolution increases proportionally to $\sin\alpha$ providing improved resolution at larger look angles. In contrast, MIMO angular resolution is maximal on-boresight and decreases off-axis due to aperture foreshortening. For this reason the beamwidth characteristics of MIMO and DBS complement each other.

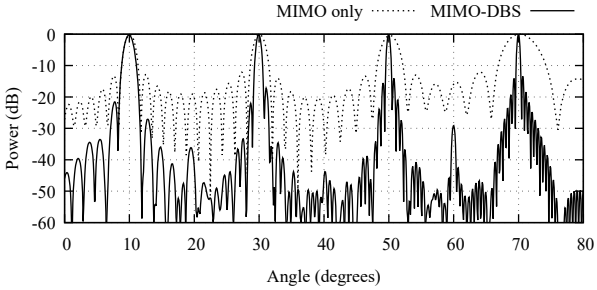

Fig. 7: Azimuth cut before and after MIMO-DBS.

In (5) we define $v_{\max}$ under the assumption that the sign of the radial velocity is unknown. When imaging stationary targets we can relax this assumption, allowing velocity to be unambiguously resolved for $v_{\mathrm{p}} \leq 2v_{\max}$. However, if v_{p} exceeds $2v_{\max}$, which may occur at high vehicle speeds due to limited PRF, the ambiguity cannot be resolved. The maximum unambiguously resolvable angular position under DBS is

$$\alpha_{\max} = \begin{cases} \arccos\left(1 - \frac{2v_{\max}}{v_{\mathrm{platform}}}\right), & \text{if } v_{\mathrm{p}} > 2v_{\max} \\ 90°, & \text{otherwise} \end{cases} \quad (11)$$

For example, for a Doppler sampling interval of 1 ms and a platform velocity of 10 mph, the maximum unambiguously resolvable angle is ±56°.

Fig. 8a shows the simulated MIMO beam pattern for a 1D horizontal array with a single target located at 30° in azimuth and 0° in elevation. Fig. 8b shows the simulated DBS beam pattern with a platform speed of 10 mph and Fig. 8c shows product of the MIMO and DBS beam patterns. True target position is shown as a black square in the figure. Relevant radar parameters are provided in Table I.

C. Theoretical performance

The expected full-width half-maximum beamwidth as a function of target position can be calculated for the MIMO and DBS cases individually, as well as for the combined MIMO and DBS case. When no weighting function is applied, the beam pattern will follow the sinc function and the 3 dB roll-off points can be calculated by solving the equations

$$\mathrm{sinc}^2\left(\left(\sin\left(\theta + \Delta\theta^{\pm}_{\mathrm{MIMO}}\right) - \sin\left(\theta\right)\right) \cdot \frac{N}{2}\right) = \frac{1}{2} \quad (12)$$

$$\mathrm{sinc}^2\left(\left(\cos\left(\theta + \Delta\theta^{\pm}_{\mathrm{DBS}}\right) - \cos\left(\theta\right)\right) \cdot \frac{v_{\mathrm{p}}}{\Delta v}\right) = \frac{1}{2} \quad (13)$$

where $\Delta\theta^{\pm}_{\mathrm{MIMO}}$ and $\Delta\theta^{\pm}_{\mathrm{DBS}}$ are the 3 dB points for the MIMO and DBS cases respectively, N is the number of virtual array elements and Δv is the velocity resolution from (4). Beamwidths are then calculated as $\Delta\theta_{\mathrm{MIMO}} = \Delta\theta^{+}_{\mathrm{MIMO}} - \Delta\theta^{-}_{\mathrm{MIMO}}$ and $\Delta\theta_{\mathrm{DBS}} = \Delta\theta^{+}_{\mathrm{DBS}} - \Delta\theta^{-}_{\mathrm{DBS}}$. These equations can then be simplified using a linear

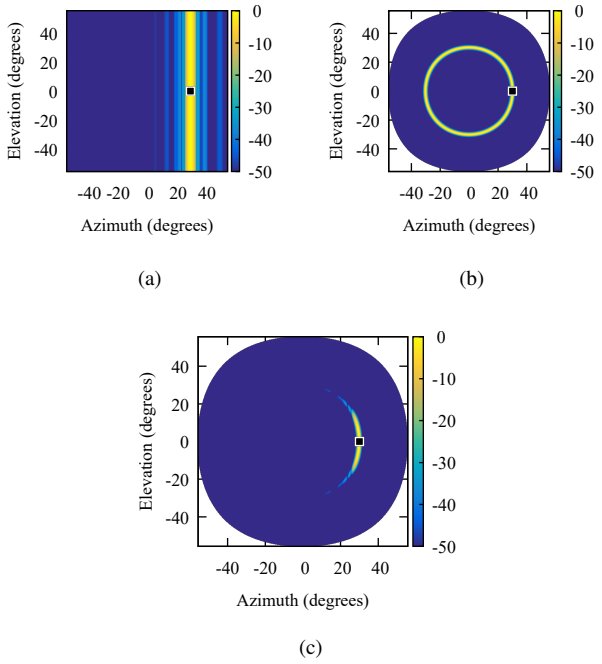

Fig. 8: Simulated antenna patterns with Hann weighting showing (a) MIMO only, (b) DBS only and (c) combined MIMO and DBS.

approximation centered at θ. By taking their product an equation for the combined MIMO-DBS case is obtained.

$$\mathrm{sinc}^2\left(\frac{N\cos\theta}{2}\Delta\theta^{\pm}\right) \cdot \mathrm{sinc}^2\left(\frac{2Tv_{\mathrm{p}}\sin\theta}{\lambda_c}\Delta\theta^{\pm}\right) = \frac{1}{2} \quad (14)$$

where $\Delta\theta = \Delta\theta^{+} - \Delta\theta^{-}$ is the overall 3 dB beamwidth. It can be shown numerically that

$$\mathrm{sinc}^2\left(ax\right) \cdot \mathrm{sinc}^2\left(bx\right) = \frac{1}{2} \quad (15)$$

has the solution $x \approx \pm 0.45/\sqrt{a^2 + b^2}$. Hence an approximation for beamwidth in the combined MIMO-DBS case is given by

$$\Delta\theta \approx \frac{0.9}{\sqrt{\left(\frac{N}{2}\cos\theta\right)^2 + \left(\frac{2Tv_{\mathrm{p}}}{\lambda_c}\sin\theta\right)^2}} \quad (16)$$

The point where MIMO-only and DBS-only beamwidths are equal is

$$\theta' = \arctan\left(\frac{N\lambda_c}{4Tv_{\mathrm{p}}}\right) \quad (17)$$

meaning that MIMO-DBS offers enhanced resolution for targets located at angles greater than θ'.

Fig. 9 shows beamwidths for MIMO, DBS and combined MIMO and DBS processing using radar parameters provided in Table I (Section IV) with no weighting function, neglecting range cell migration. Beamwidth was calculated numerically to obtain an exact result. It can

be seen that on-boresight, combined resolution is exactly equal to the inherent MIMO resolution. The transition point θ' is at 6.1°, indicated by a dashed vertical line. Off-axis, DBS greatly enhances the angular resolution. It should be noted that the reduction in beamwidth seen near-boresight occurs in the DBS case due to one of the 3 dB roll-off points extending beyond the platform velocity in the Doppler dimension. From (8) it can be seen that α is not well defined for $|v_{\mathrm{r}}| > |\boldsymbol{v}_{\mathrm{p}}|$, hence we instead clamp α to 0°, thus causing a reduction in measured beamwidth close to boresight.

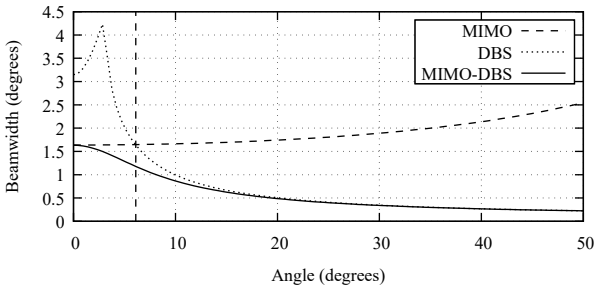

Fig. 9: 3 dB beamwidths for MIMO, DBS and MIMO plus DBS versus azimuth angle, without weighting.

D. Range cell migration

DBS beamwidth benefits from an increased integration period. Furthermore, in order to achieve a suitable SNR, particularly for detection of terrain and other low-RCS targets it is necessary to integrate over a sufficiently long period. Range cell migration will however impose an upper limit on DBS performance. The number of range cells traversed by a target is

$$N = \frac{2B}{c} v_{\mathrm{p}} T \cos\alpha \tag{18}$$

where B is the chirp bandwidth. For example, a target at 25° migrates through 7 range cells for a platform velocity of 10 mph, a bandwidth of 2 GHz and an integration period of 128 ms. As the target transits though a given range cell, the effect on the target radar signal is equivalent to the application of a narrow weighting function, resulting in an coarsening of MIMO-DBS resolution. As a result, there will be a critical value of T, depending on FMCW bandwidth, beyond which the cross-range resolution will not be improved further. Fig. 10 shows the simulated change in beamwidth as a function of bandwidth, without weighting. As bandwidth is increased, beamwidth is enlarged due to increased range cell migration. In this way, optimal cross-range resolution will require a careful trade-off between range resolution and cross-range resolution. It should be noted that it might be desirable to increase the CPI further in order to provide optimal SNR.

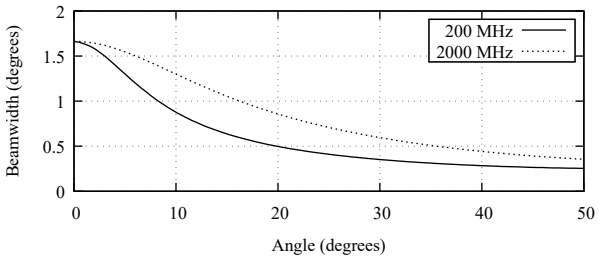

Fig. 10: Numerically calculated beamwidth versus target azimuth position, accounting for range cell migration.

E. Platform velocity accuracy

Since DBS requires knowledge of the platform velocity, it is important to quantify the accuracy required in order to ensure acceptable performance. An error in the platform velocity estimate will result in a corresponding error in the estimated angular position. Furthermore, under MIMO-DBS processing this discrepancy will result in a loss of power when the MIMO and DBS beam patterns diverge. By rearranging (8), an expression for the angle error can be obtained.

$$\epsilon_\theta = \arccos\left(\frac{v_{\mathrm{p}}}{v_{\mathrm{p}} + \epsilon_v}\cos\theta\right) - \theta \tag{19}$$

where ϵ_v is the error in the platform velocity estimate. This equation can be simplified using a first-order Taylor series approximation at $\epsilon_v = 0$.

$$\epsilon_\theta \approx \frac{\epsilon_v}{v_{\mathrm{p}} \tan\theta} \tag{20}$$

For cross-range positions where DBS beamwidth is much smaller than MIMO beamwidth, loss of power will be limited to 3 dB if ϵ_v is constrained so as to ensure that the DBS azimuth position estimate lies within the MIMO beamwidth. By combining (20) with the component of MIMO beamwidth from (16) a constraint on the maximum allowable error can be obtained.

$$\frac{\epsilon_v}{v_{\mathrm{p}}} \leq \frac{0.9\tan\theta}{N\cos\theta} \tag{21}$$

Fig. 11 shows the maximum allowable percentage error as a function of target azimuth position and the error in the angular position estimate corresponding to a 1% error. This suggests that power loss will not exceed 3 dB for angles above 20° if a 0.5% estimate accuracy is achieved, or for angles above 30° if a 1% estimate accuracy is achieved.

This simple analytic expression in (21) will tend to overestimate the required accuracy for positions closer to boresight, where DBS beamwidth is similar to or greater than the MIMO beamwidth.

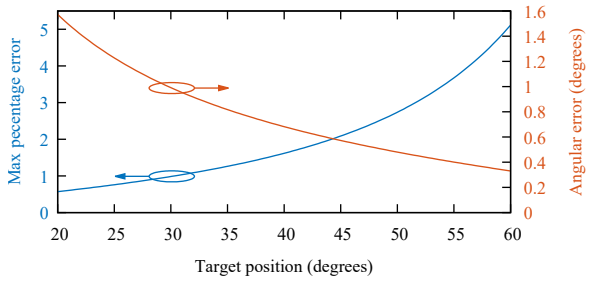

Fig. 11: Plot showing the required percentage error in platform velocity (left axis) and the angular error for a 1% error in the platform velocity estimate (right axis).

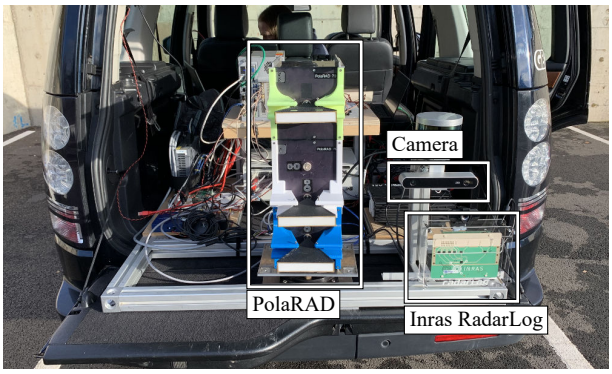

Fig. 12: Photograph of the on-vehicle experimental setup incorporating the Inras RadarLog, PolaRAD and camera.

IV. SIMULATION AND EXPERIMENTAL RESULTS

A. Radar hardware

The experimental work described in this section was performed with an Inras RadarLog sensor with a 77 GHz 4RX/16RX MIMO frontend [18]. Due to the limited USB bandwidth available for transferring data, chirp parameters were carefully optimized to achieve suitable range resolution and maximum unambiguous range while maintaining an adequate maximum unambiguously resolvable velocity, assuming a platform velocity of up to 15 mph. In order to provide a close-to-ideal radar image for the purpose of comparison data was recorded simultaneously using our PolaRAD 79 GHz mechanically steered real aperture wideband radar with fan-beam antennas. The relevant operating parameters are provided in Table I.

TABLE I: Operating parameters for both radars

Parameter	RadarLog	PolaRAD	Units
Modulation	FMCW	FMCW	—
Center frequency (f_c)	77	78.5	GHz
Bandwidth (B)	2	5	GHz
Sample rate	10	40	MSa/s
Samples per chirp	2048	80000	—
Chirp duration	204.8	2000	µs
Chirp interval (T_{chirp})	230	5500	µs
MIMO frame interval (T_{MIMO})	1	—	ms
Frame interval (T)	128	1040	ms
Range resolution	7.5	3	cm
Velocity resolution	±0.015	—	m/s
Max. unambiguous range	76.7	600	m
Max. unambiguous velocity	±0.97	—	m/s
Beamwidth	1.7	1.7	°

PolaRAD was mounted on a mechanical turntable and scanned over a 60° FOV using stepper motor and worm gear. The radar was chirped at each angular position in sync with the stepper pulses, with a total frame scan time of approximately 1 s. For this reason, Doppler processing is not feasible. Furthermore, due to the large size of PolaRAD, it was not possible to mount these radars on the front of the vehicle so the radars were instead directed out of the rear of the vehicle as shown in Fig. 12.

During measurement the vehicle was driven in the forward direction at speeds in the range of 5-15 mph. At such speeds, distortion of the resulting plan position indicator (PPI) due to the rolling shutter effect is observed, but is manageable.

For consistency, identical parameters were used for both simulation and experimental measurement. In both cases, the resulting data was processed using the same MATLAB implementation of the MIMO-DBS algorithm described in Section III.

B. Simulation results

As a proof-of-concept to validate expected performance, synthetic radar data was created using MIMO simulation software written in MATLAB. The simulated antenna geometry was equivalent to the antenna geometry of the Inras RadarLog 4TX/16RX frontend.

A resolution test was performed using a series of 35 ideal point targets arranged on a regularly spaced grid with a separation of 5 m from -15 m to 15 m in cross-range and 30 m to 50 m in range and an elevation angle of 0°. Platform motion was set to 10 mph.

Simulations were performed for a baseline measurement with no platform motion (Fig. 13a), for platform motion at 10 mph with no processing (Fig. 13b), for motion at 10 mph with motion compensation only (Fig. 13c) and for motion at 10 mph with both motion compensation and DBS (Fig. 13d).

Without correction, motion-induced degradation is severe. After motion compensation is applied the azimuthal degradation is substantially reduced. However, a reduction in the effective range resolution is observed due to range cell migration. After MIMO-DBS processing is applied, the anticipated improvements in beamwidth are readily apparent, particularly for targets which lie furthest off-axis. A reduction in side-lobe levels is observed as expected.

C. Experimental imaging results

Experimental results were gathered in two locations on the University of Birmingham campus. An accurate direct measurement of platform velocity was not available for

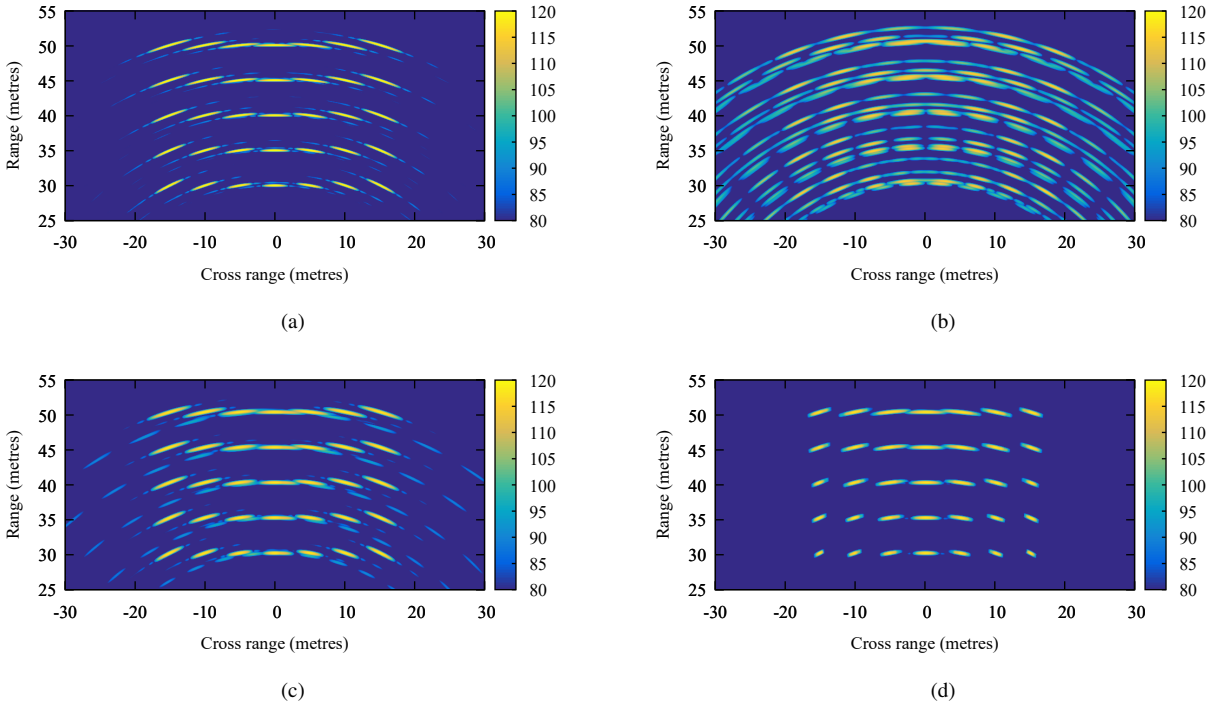

Fig. 13: Simulation results using MIMO-only for (a) stationary platform, for moving platform (b) without motion correction and (c) with motion correction and (d) for moving platform using full MIMO-DBS.

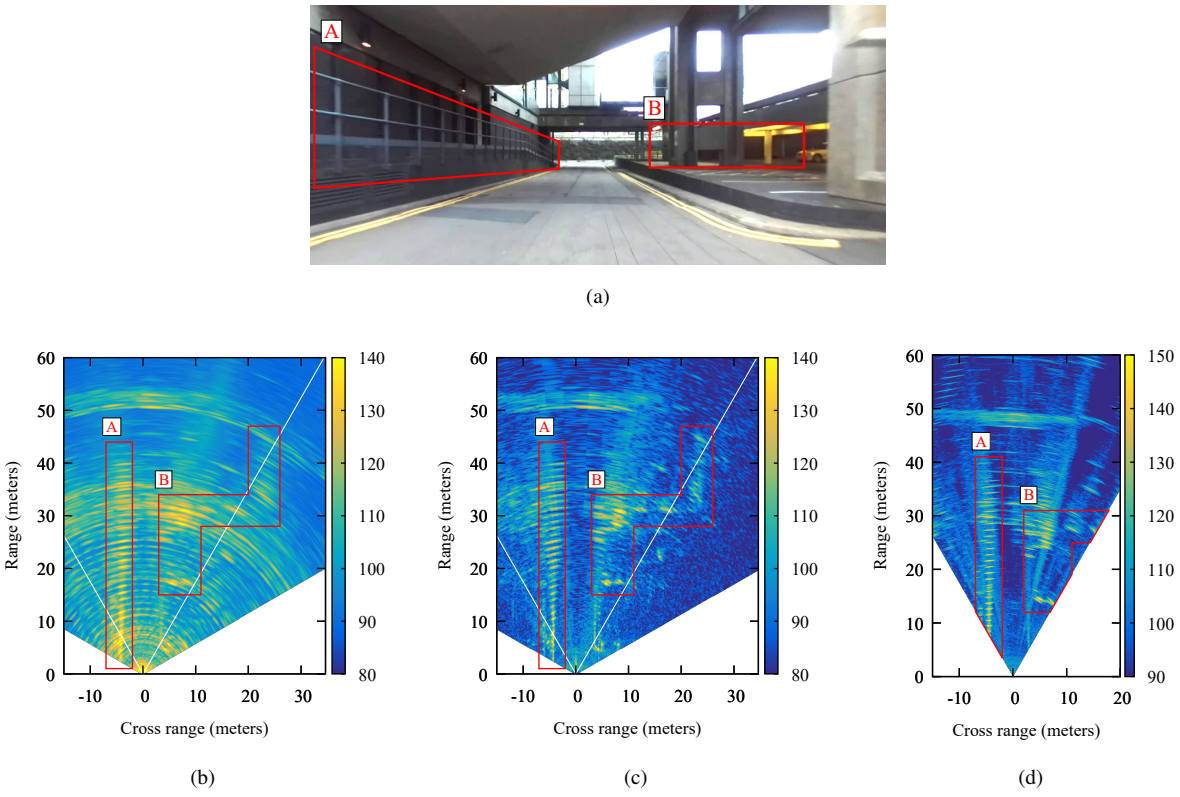

Fig. 14: Results of applying MIMO-DBS processing to on-vehicle measured data taken under Muirhead tower on UoB campus [19] showing a) photograph of the scene, b) MIMO image after motion correction, c) MIMO-DBS image and d) PolaRAD image. Results after MIMO-DBS processing are comparable to the mechanically steered radar.

these experiments. In order to process these recorded data, an estimate of the platform velocity was obtained through an initial estimation from Doppler returns, followed by a manual autofocus to deliver the best resolution. During the process of manual adjustment, the accuracy required for optimal image quality was observed to be consistent with the theoretical constraint on accuracy presented in Section III-E. This is analyzed qualitatively in greater detail in Section IV-D

Fig. 14 shows example radar data obtained from these instruments, before and after correction. It can be seen that, after MIMO-DBS processing, there is a marked decrease in side-lobe levels and a substantial increase in azimuth resolution is observed, as anticipated, allowing fine detail from the scene to be resolved. Two notable regions are highlighted on the photograph and overlaid on the radar plots. In region A, to the left of the scene, a series of regularly spaced railings are visible. The cross-range resolution increases close to the radar due to the increased angle from boresight. In region B, support pillars and the back wall of the covered parking area are visible. Due to side-lobe suppression, contrast is substantially improved and the wall is clearly visible. In comparison, in the MIMO only case, only the brightest scatterers are visible and cross-range resolution is poor. As a result, the distributed nature of this feature is not evident.

Overall image quality can be seen to be comparable to the ideal benchmark system. This demonstrates that high fidelity environmental imaging is achievable, even when using lower-cost and highly compact MIMO radars. Authors have made the raw data from which these processed results were generated available through the University of Birmingham eData Repository [19].

D. Experimental resolution and error results

In order to provide validation of the theoretical resolution outlined in Section III-C, data was recorded as the vehicle was driven at 22 mph, passing a 17.8 dBsm corner reflector which was placed to the left of the vehicle trajectory and supported on a wooden tripod. To eliminate the effect of range cell migration, bandwidth was reduced to 500 MHz and a CPI of 32 ms was used. Measurements were recorded for angular positions between 10° and 31°.

Fig 15 shows the beamwidth extracted using both MIMO only and MIMO-DBS processing. Theoretical results are presented according to (16). Close agreement is observed between the experiment and theory. A small deviation around 14° is observed in the MIMO only case, however this is understood to be an artifact of the measurement setup.

In order to provide validation of the expected effects of platform velocity error outlined in Section III-E, corner reflector data recorded at 31° was used. Fig. 16a shows the angle error observed as a function of percentage velocity error. Good agreement is observed when compared to the full and simplified theoretical values obtained using (19) and (20).

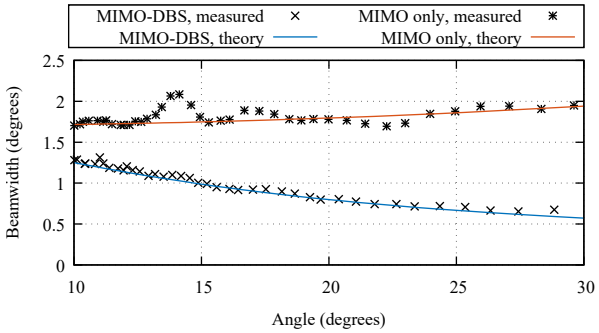

Fig. 15: Experimental measurement of beamwidth for MIMO only and MIMO-DBS.

Fig 16b shows the loss of target power observed as a function of percentage velocity error. The required accuracy to maintain a maximum 3 dB loss of target power was measured at $\pm 1.08\%$. This is comparable to the theoretical value of $\pm 1.03\%$ calculated using (21).

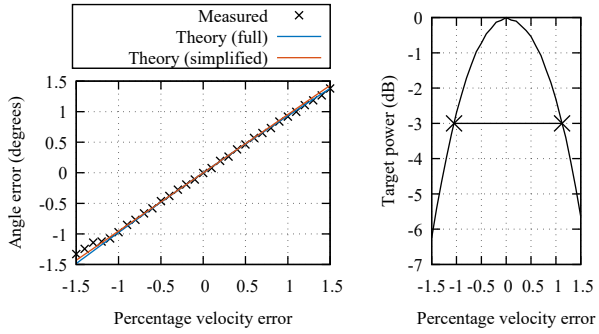

Fig. 16: Experimental measurement of a target located at 31°. Showing a) angle error as a function of percentage velocity error and b) target power as a function of percentage velocity error.

E. Coherent integration period

By increasing the coherent integration period, cross-range resolution is increased. Overall SNR is also increased, which is important when imaging low-SNR and distributed targets such as terrain. However, excessively long integration periods increase latency and reduce the effective range resolution due to range cell migration.

Fig. 17 shows the increase in SNR and angular resolution as the coherent integration period is increased from 16 ms to 128 ms. A significant improvement is observed in (c) when compared to (b), however the improvement between (c) and (d) is less pronounced. The suppressive effect of DBS on MIMO sidelobes is visible for the corner reflector located at position (0 m, 30 m). Additionally, the

curved section of wall visible in the lower right quadrant is far more clearly resolved.

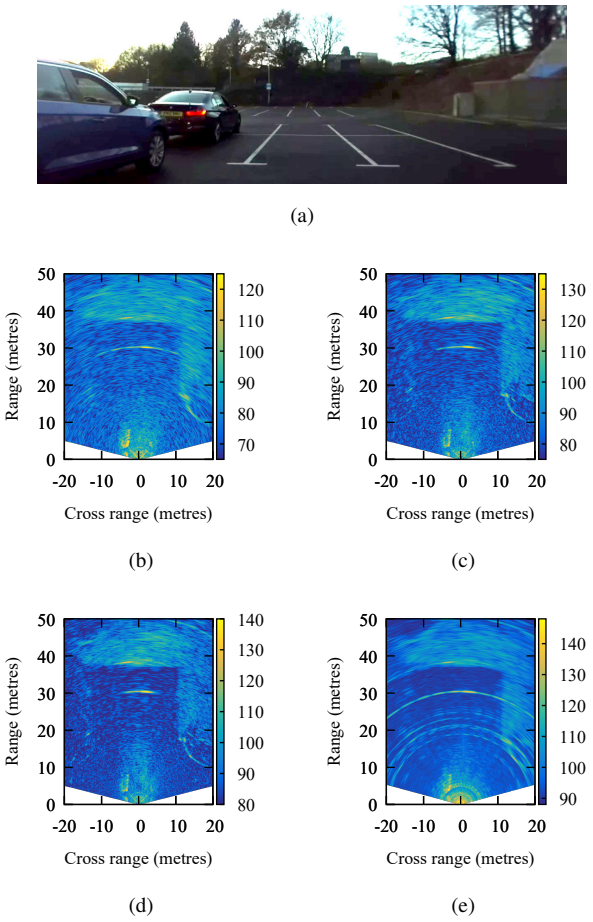

Fig. 17: Imagery from a car park scene [19] showing a) photograph, MIMO-DBS for an integration period of b) 16 ms, c) 64 ms and d) 128 ms and e) motion-corrected MIMO only for an integration period of 128 ms. Terrain returns from a grass verge are visible at the top and right hand regions of the image.

V. CONCLUSIONS

In this paper we have demonstrated that high-fidelity imaging of the stationary environment surrounding a moving vehicle can be achieved using a conventional MIMO sensor, with results which are comparable to a mechanically steered radar. Our DBS-based approach was validated through simulation and experiment using data recorded on a moving vehicle. These results indicate that advanced functionality, such as image segmentation and region classification, should be achievable in a form factor which is suitable for integration on a commercially produced vehicle.

By applying DBS, the target radial velocity is used as an indirect measurement of angle. When combined with the conventional MIMO angle-of-arrival, a single joint azimuth measurement is obtained, with a significant reduction to beamwidth across the majority of the radar FOV. Furthermore, since DBS and MIMO sidelobes do not generally overlap significantly, sidelobes are also suppressed. In the system studied in this paper, the maximum sidelobe level was reduced from -13 dB to -30 dB after MIMO-DBS processing with no weighting. Application of weighting may further reduce sidelobe levels, but at the expense of reduced cross-range resolution.

An analysis was performed yielding theoretical expressions for the expected MIMO-DBS beamwidth as a function of array size, platform velocity and coherent integration period. Additionally, expressions were obtained for the expected error in angular position and target power due to errors in the platform velocity estimate. These performance analyses were confirmed experimentally using measurements of a reference corner reflector. As range resolution is increased, cross-range resolution decreases due to a reduction in the effective coherent processing interval as the result of range cell migration. Increased platform velocity will also result in increased range cell migration.

Due to limitations in the specific MIMO sensor used in our experimental setup, particularly with regards to available USB bandwidth, the maximum unambiguous velocity was relatively low. In a purpose-built sensor it would be feasible to increase the unambiguous velocity significantly by increasing the PRF, allowing for increased platform velocities.

The optimal radar parameters depend strongly on the situation in which the sensor is operating. For example, high cross-range resolution is most important at larger slant ranges due to expansion of the beam. In such situations it would be useful to sacrifice some range resolution to improve cross-range resolution. For this reason, MIMO-DBS is likely to benefit from a cognitive approach, with operating parameters selected and refined depending on platform velocity, required sensing range and the specific driving environment.

This paper only considered the application of MIMO-DBS in the presence of a stationary background environment. Future work will consider the extension of this technique to environments containing dynamic actors in addition to the stationary background.

REFERENCES

[1] D. M. Grimes and T. O. Jones, "Automotive radar: A brief review," *Proceedings of the IEEE*, vol. 62, no. 6, pp. 804–822, 1974.

[2] S. M. Patole, M. Torlak, D. Wang, and M. Ali, "Automotive radars: A review of signal processing techniques," *IEEE Signal Processing Magazine*, vol. 34, no. 2, pp. 22–35, 2017.

[3] I. Bekkerman and J. Tabrikian, "Target detection and localization using MIMO radars and sonars," *IEEE Transactions on Signal Processing*, vol. 54, no. 10, pp. 3873–3883, 2006.

[4] T. Mitomo, N. Ono, H. Hoshino, Y. Yoshihara, O. Watanabe, and I. Seto, "A 77 GHz 90 nm CMOS transceiver for FMCW radar applications," *IEEE Journal of Solid-State Circuits*, vol. 45, no. 4, pp. 928–937, 2010.

[5] I. Bilik, O. Longman, S. Villeval, and J. Tabrikian, "The rise of radar for autonomous vehicles: Signal processing solutions and

future research directions," *IEEE Signal Processing Magazine*, vol. 36, no. 5, pp. 20–31, 2019.
[6] L. Daniel, D. Phippen, E. Hoare, A. Stove, M. Cherniakov, and M. Gashinova, "Low-THz radar, lidar and optical imaging through artificially generated fog," in *International Conference on Radar Systems (Radar 2017)*, 2017, pp. 1–4.
[7] Y. Xiao, L. Daniel, and M. Gashinova, "Image segmentation and region classification in automotive high-resolution radar imagery," *IEEE Sensors Journal*, vol. 21, no. 5, pp. 6698–6711, 2021.
[8] C. M. Schmid, C. Pfeffer, R. Feger, and A. Stelzer, "An FMCW MIMO radar calibration and mutual coupling compensation approach," in *2013 European Radar Conference*, 2013, pp. 13–16.
[9] H. Sun, F. Brigui, and M. Lesturgie, "Analysis and comparison of MIMO radar waveforms," in *2014 International Radar Conference*, 2014, pp. 1–6.
[10] F. Roos, J. Bechter, N. Appenrodt, J. Dickmann, and C. Waldschmidt, "Enhancement of Doppler unambiguity for chirp-sequence modulated TDM-MIMO radars," in *2018 IEEE MTT-S International Conference on Microwaves for Intelligent Mobility (ICMIM)*, 2018, pp. 1–4.
[11] J. Bechter, F. Roos, and C. Waldschmidt, "Compensation of motion-induced phase errors in TDM MIMO radars," *IEEE Microwave and Wireless Components Letters*, vol. 27, no. 12, pp. 1164–1166, 2017.
[12] C. M. Schmid, R. Feger, C. Pfeffer, and A. Stelzer, "Motion compensation and efficient array design for TDMA FMCW MIMO radar systems," in *2012 6th European Conference on Antennas and Propagation (EUCAP)*, 2012, pp. 1746–1750.
[13] M. I. Skolnik, *Radar Handbook: 3rd Edition*. New York: McGraw-Hill, 2008.
[14] M. E. Radant, "The evolution of digital signal processing for airborne radar," *IEEE Transactions on Aerospace and Electronic Systems*, vol. 38, no. 2, pp. 723–733, 2002.
[15] A. Laribi, M. Hahn, J. Dickmann, and C. Waldschmidt, "A new height-estimation method using FMCW radar Doppler beam sharpening," in *2017 25th European Signal Processing Conference (EUSIPCO)*, 2017, pp. 1932–1396.
[16] L. Daniel, A. Stove, E. Hoare, D. Phippen, M. Cherniakov, B. Mulgrew, and M. Gashinova, "Application of Doppler beam sharpening for azimuth refinement in prospective low-THz automotive radars," *IET Radar, Sonar & Navigation*, vol. 12, no. 10, pp. 1121–1130, 2018.
[17] Jaguar Land Rover Ltd., "Improving MIMO radar with Doppler beam sharpening," United Kingdom Patent Application GB2 203 243.7, 03 09, 2022.
[18] Inras RadarLog website. Accessed: 2022-04-13. [Online]. Available: https://inras.at/en/radarlog/
[19] University of Birmingham CORTEX Repository: Campus Driving MIMO Dataset. [Online]. Available: https://doi.org/10.25500/edata.bham.00000825

Scott L. Cassidy received the Ph.D. degree in Physics in 2015 from the University of St Andrews. He has wide range of experience in FMCW radar at millimeter and sub-millimeter frequencies in a number of different applications, including short-range and long-range remote sensing and standoff detection of concealed objects. In 2016 he joined the Microwave Integrated Systems Laboratory (MISL) at the University of Birmingham, UK, where he is currently a research fellow. His current research is focused on the advancement of millimeter wave radar and MIMO techniques in automotive sensing.

Sukhjit Pooni received the Ph.D. degree in radar system, in 2017, from the University of Birmingham, UK. Prior to this he was a RF Systems Engineer at ST-Ericsson. His PhD research was on the subject of MIMO radar sensing on a towed antenna array. His research interests include MIMO radar systems, automotive radar systems and cognitive radar techniques. He is currently a post-doctoral researcher in the Microwave Integrated Systems Laboratory (MISL), University of Birmingham, UK.

Mikhail Cherniakov graduated from Moscow Technical University in 1974. He received the Ph.D. degree in 1980 and the D.Sc. degree in 1992. He was a Full Professor in 1993. In 1994, he was a Visiting Professor with the University of Cambridge. In 1995, he moved to the University of Queensland, Australia. In 2000, he joined the School of EESE, Birmingham. Here, he founded the Microwave Integrated Systems Laboratory. He is the Chair of the Aerospace and Electronic Systems, University of Birmingham, U.K, with more than 40 years experience on the R&D in radar systems. His research interests are in forward scatter and multistatic radar, active and passive radar, automotive, and short range sensors. He is the author/editor/coauthor of five books. He has more than 250 peer-reviewed publications. In 2017, he received the Christian Hülsmeyer Award for his achievements in radar research and education.

Edward G. Hoare received the Ph.D. degree in over-the-horizon radar from the University of Birmingham. He undertook an apprenticeship at the Royal Radar Establishment, College of Electronics, Malvern, U.K., and after a spell in industry, he joined the School of Electronic, Electrical, and Computer Engineering, University of Birmingham. Since then, he has been involved in teaching, design, and research into radar systems and antennas covering frequencies from 2 MHz to over 670 GHz, including non-co-operative bistatic radar, atmospheric radar acoustic sounding, automotive radar, and low-THz radar. Over the past 12 years, he has provided antenna and millimeter-wave radar consultancy to Jaguar Land Rover and Ford Motor Company. He holds a number of patents in automotive radar. He was a member of the European Automotive Radar Standards Group.

Marina S. Gashinova received the M.Sc. degree in math from Saint Petersburg State University in 1991, and the Ph.D. degree in physics and math from Saint Petersburg Electrotechnical University, Russia, in 2003. In 2006, she joined the Microwave Integrated System Laboratory (MISL), University of Birmingham (UoB), where she is the Chair of Pervasive Sensing. She is also the Head of the Pervasive Sensing Group, MISL, leading a number of research projects on automotive sensing and THz sensing. Her area of interests include active and passive radar, imaging THz sensing for ground and spaceborne scene assessments, cognitive radar, and deep neural networks classification.